

Multi-scale investigation of dislocation mediated carbon migration in iron

Tigany Zarrouk

August 8, 2020

Contents

1	Introduction	2
2	Computational Method	4
2.1	Peierls Potential	4
2.2	Preliminary calculations	6
2.3	Fe-C binding energies	7
2.4	Analysis of carbon concentration along dislocation	7
2.5	Progression to Line Tension Model	8
3	Results	8
3.1	Peierls Potential	8
3.2	Preliminary calculations	10
3.3	Fe-C binding energies	10
3.4	Analysis of carbon concentration along dislocation	15
3.5	Progression to Line Tension Model	18
4	Discussion	18
5	Future work	20
6	Conclusion	21
7	Appendix	22
7.1	Regularisation of interaction energy in quadrupolar array . . .	22
7.2	Zero-point energy calculation	22
8	Bibliography	23

1 Introduction

Martensitic steels are frequently used in bearings due to their resilience to service conditions, being subject to high rotational speeds and contact pressures. However, under cyclic loading exceeding a given contact stress, the microstructure of the steel can decay due to the accumulation of plasticity. This signals the onset of rolling cycle fatigue (RCF), which increases the risk of failure from subsurface crack initiation. The microstructural decay corresponds to the observation of Dark Etching Regions (DERs) as seen in optical microscopy, where the darkness of these regions is due to the higher reactivity of the phases which compose the DER to the etchant; exacerbated by the roughness of the DER region, see figure 1.

Carbon within the martensitic matrix at normal operating temperatures has a low diffusivity; as such, segregation by diffusion of carbon out of the martensite is limited. A plausible mechanism for the degradation of the martensitic microstructure is a process of carbon migration, driven by dislocation glide [1, 2, 3, 4, 5, 6]. Due to the high dislocation density exhibited in martensite, carbon segregates to dislocations in Cottrell atmospheres, causing pinning. Strain generated by cyclic stresses allow dislocations to escape their carbon rich environment. The freed dislocations re-attract carbon, allowing the Cottrell atmosphere to reform, subsequently re-pinning the dislocations, creating a net carbon flux.

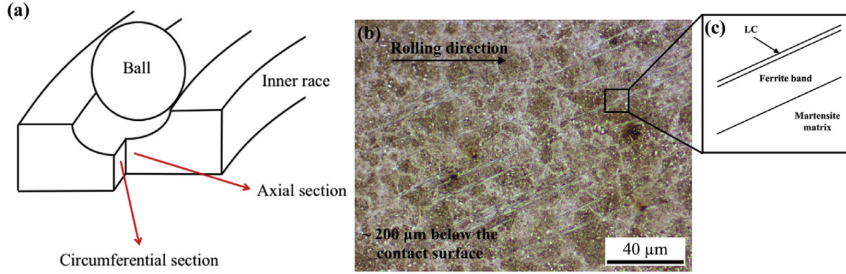


Figure 1: Diagram of where DER occurs and its characteristics, taken from [1]. (a) Axial and circumferential sections of a bearing inner ring. (b) Circumferential section of a bearing inner ring under optical microscope, where ferrite bands (white etching bands) are formed at the subsurface with an inclination angle of 30° to the rolling direction. (c) Diagram showing the structure of a WEB consisting of a ferrite band and a LC adjacent to it. One can see the DER region is composed of regions of ferrite interspersed in the parent martensite with lenticular carbides bordering the ferrite bands.

Through dislocation-assisted carbon migration, martensite transforms to ferrite (microband and elongated forms). Residual carbides, untouched at the start of DER formation, gradually dissolve as a result of highly localised

plasticity: dislocation rearrangement and pile ups at the interface draw carbon atoms out. Further RCF progression leads to the formation of low and high angle ferrite features, White Etching Bands (WEBs), composed from the microband and elongated ferrite. Dislocation motion allows carbon to move from the martensitic matrix—and (partially) dissolved residual carbides—to form lenticular carbides between these ferrite bands.

However, fundamentals behind DER formation through this process remain contentious. It is not definitively known where carbon migrates to with the onset of DER formation: where does excess carbon from the martensitic matrix find itself, when the structure decays to low solubility (0.02 wt\% towards the residual transition carbides, [2], or if they segregate to the boundaries of ferrite microbands/elongated ferrite.

Fu *et al.* propose that carbon atoms inside the martensite would segregate to pre-existing/residual carbides, increasing their size [2]. This theory has been successfully applied to the growth of lenticular carbides [1], however, problems arise with their application to the growth of residual carbides: if carbides were to form in martensite, they should follow the Bagaryatskii/Isaichev orientation relationship, but observations suggest a lack of any orientation relationship [7]. Carbides formed within the DER region have an irregular shape/diffuse boundaries, which are seemingly due to the incomplete *dissolution* of *residual* carbides, which is at odds with the theory of Fu *et al.* and residual carbide growth.

Probing the fundamental mechanisms behind DER formation experimentally have proven difficult and inconclusive. Work needs to be done to understand dislocation-carbon interactions, more specifically: how dislocations can move carbon within the temperature and stress regimes experienced during operation; where carbon is transported to and what the resulting dislocation network would be. This is vital to understanding martensite decay and DER formation. With further knowledge of the fundamental mechanism behind DER formation, we can suppress dislocation motion in the martensitic matrix, mitigating failure by RCF.

To shed light dislocation-assisted carbon migration, a multi-scale modelling approach can be used. Atomistics can provide information of the 2d Peierls energy landscape which dislocations are subject to in iron; and how this landscape is modified by the binding of carbon to dislocations. This data can be used in a line tension model of a dislocation, to determine the kink-pair nucleation energies of dislocations as a function of carbon content and stress. Finally, one can use a kinetic Monte Carlo (kMC) model of dislocation glide, by thermally activated kink-pair nucleation, in an environment of carbon. From this last stage of coarse-graining, one can determine in which regimes of temperature, stress and carbon concentration, dislocation-assisted carbon migration becomes a feasible mechanism behind DER formation, with predictions of dislocation velocity, dislocation configurations and where carbon moves to with dislocation movement. In this report, we

will focus on the atomistic portion of this project, directed at understanding dislocation-carbon interactions at the atomistic scale in bcc iron, of which results will feed into the line-tension and kMC models.

2 Computational Method

We use the tight-binding model of Paxton and Elsätter [8], which has been shown to describe the binding energies of carbon complexes in bcc iron in good agreement with Density Functional Theory (DFT) calculations. This model reproduces the two screw dislocation core structures—the easy and hard $1/2\langle 111 \rangle$ cores—exhibited in bcc iron, which are crucial to understanding solute-dislocation interactions in bcc iron. Hydrogen and carbon have been shown to reconstruct these cores into the, usually metastable, hard core from the easy core [9, 10]. Computationally cheaper models, which do not incorporate quantum mechanics, such as the EAM, cannot reproduce these behaviours.

2.1 Peierls Potential

To determine the Peierls potential of a $1/2\langle 111 \rangle$ screw dislocation, we followed the procedure detailed in Itakura [11]. Quadrupolar arrays of dislocations were constructed by placing dislocations of antiparallel $1/2\langle 111 \rangle$ Burgers vectors in an "S" arrangement [12], see figure 2, with initial displacements determined by the anisotropic elasticity solutions. These displacements were modified to be periodic, thereby removing artificial stacking faults which would appear between periodic images after the introduction of the dislocation dipole. This was achieved by the subtraction of a linear error term from the superposition of displacement fields arising from the dislocations in the simulation cell and its periodic images [13]. To accommodate for the internal stress upon introduction of the dislocation dipole into a simulation cell, an elastic strain was applied to the cell, resulting in an additional tilt component added to the cell vectors [12, 13]. Simulation cells were constructed with different initial core positions, which were sampled from the triangular region "EHS" (easy, hard and split) core positions, as detailed in figure 3. To fix the dislocation positions during relaxation, the three atoms surrounding the easy core, for each dislocation, were fixed in Z coordinate during relaxation, where Z is a $\langle 111 \rangle$ direction. The k-point sampling mesh for each of these cells was $5 \times 5 \times 30$.

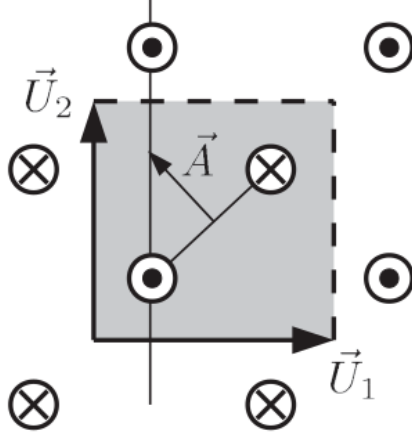


Figure 2: Figure of the quadrupolar arrangement used to determine the Peierls potential. \vec{U}_1 and \vec{U}_2 are the periodicity vectors in the X-Y plane. \vec{A} is the vector defining the cut plane of the dislocation dipole [12].

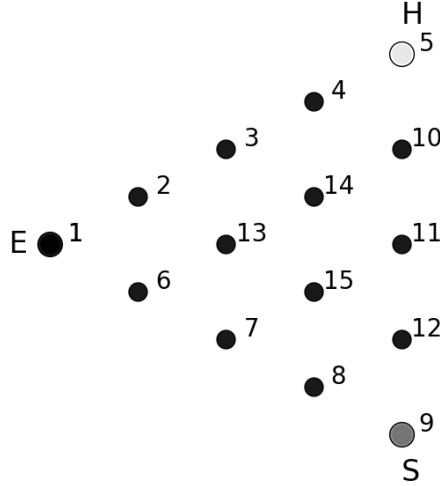


Figure 3: Figure of the sampled positions used to determine the the Peierls potential. "E", "H" and "S" correspond to the easy, hard and split core positions respectively.

The interaction energy between the dislocation dipole and periodic images was defined differently to that of Itakura's. We followed the prescription of Bulatov and Cai [13] to find a regularised interaction energy, which is independent of truncation limit, in contrast to the formulas quoted in Itakura's papers [11]. Details can be found in section 7.1.

The Peierls potential here is defined relative to the energy of a relaxed easy core configuration

$$\Delta E_P = \Delta E^{\text{tbe}} - \Delta E_{\text{INT}}, \quad (1)$$

where Δ refers to quantities relative to the easy core configuration, divided by the total number of dislocations in the reference cell. The difference in total energies is taken between a relaxed cell with displaced dislocation cores, from the periodic easy core reference, with a correction term coming from the difference in interaction energies between periodic images between the displaced dislocation cell and the reference, ΔE_{INT} .

2.2 Preliminary calculations

To determine the binding energy of carbon to dislocations, we used the cluster method: simulation cells consisted of a cylindrical cluster of atoms, with a single dislocation introduced into the centre using displacements from anisotropic elasticity solutions. Each of the clusters were centred on the easy or hard core positions. The cluster of atoms was split into two regions: a central region of dynamic atoms with radius R_1 , and an annulus of atoms, between R_1 and R_2 , which were fixed in position to the anisotropic elasticity solutions.

To confirm the anisotropic elasticity solutions we were using was correct, we compared the displacements against the analytic solutions to the straight screw dislocation, as given in Hirth and Lothe [14]. Furthermore, energy scaling relations were verified. We inserted dislocation into cells of varying radii: $R_1 = x\sqrt{2}a_{\text{bcc}}$, and $R_2 = (x + 1)\sqrt{2}a_{\text{bcc}}$, where $x \in \{2 \dots 5\}$. The excess energy was defined as the energy difference of a cell with a dislocation inserted, E_{d} , with respect to a perfect cell reference energy of the same geometry,

$$E_{\text{excess}} = E_{\text{core}} + E_{\text{elastic}} = E_{\text{d}} - E_{\text{perfect}}, \quad (2)$$

where $E_{\text{elastic}} = (\mu b^2/4\pi)\ln(R/r_c)$, with $R = R_2$ and $r_c = b$.

Initially, large cells of with $R_1 = 6\sqrt{2}a_{\text{bcc}}$, and $R_2 = 7\sqrt{2}a_{\text{bcc}}$ and depth of single burger's vector, were relaxed for both the easy and hard cores, which consisted of 522 and 540 atoms respectively. The three atoms surrounding the core were constrained to only relax in $X - Y$ plane, to fix the dislocation upon relaxation. The k-point sampling mesh for each of these cells was $1 \times 1 \times 24$.

From the relaxed cells, a smaller region of 174 atoms, with $R_1 = 3\sqrt{2}a_{\text{bcc}}$, and $R_2 = 4\sqrt{2}a_{\text{bcc}}$, was cut from the dynamic regions. This smaller cell was extended to a thickness of $3b$ in the Z direction. Carbon interstitials were inserted into octahedral sites near the dislocation core, in the middle layer. Exploiting reflection and rotational symmetry, allows us to use only 10 interstitial sites to obtain the binding energies of carbon ~ 2 b from the core, denoted by iHj and iEj , where $j \in \{1 \dots 10\}$.

The three atoms surrounding the core in the first and third layers were again constrained to relax only in the X and Y directions. No such constraints were imposed on the middle layer.

2.3 Fe-C binding energies

Following the paper by Itakura [10] we calculated the binding energy of carbon each of the screw dislocation cores.

The binding energy is given by

$$E_b = E_{d+C} + E_{\text{Perfect}} - E_d - E_{C \text{ ref.}}, \quad (3)$$

where E_{d+C} is the total energy of a relaxed cluster with a carbon interstitial and a dislocation, E_d is the total energy of a relaxed cluster with a dislocation and $E_{C \text{ ref.}}$ is the total energy of a relaxed perfect cluster with a single carbon in an octahedral site.

The zero-point energy (ZPE) is calculated as in Itakura, details can be found in 7.2. The ZPE corrected binding energy is given by

$$E_b^Z = E_b + \Delta E_z,$$

where $\Delta E_z = E_z - E_{zC \text{ ref.}}$ and $E_{zC \text{ ref.}} = 202.5 \text{ meV}$ is the zero-point energy of carbon situated in an octahedral site in a perfect cluster of the same size.

2.4 Analysis of carbon concentration along dislocation

Using the Fe-C binding energies, one can predict the equilibrium carbon concentration of a carbon binding site c_d , under the assumption that carbon atoms around the core are sufficiently spaced such that intersite interaction energies are negligible [9].

The concentration is given by

$$\frac{c_d^i}{1 - c_d^i} = \frac{c_{\text{bulk}}}{1 - c_{\text{bulk}}} \exp\left(\frac{E_b^i}{k_B T}\right), \quad (4)$$

where i denotes the i^{th} carbon binding site (with the convention of attraction denoting a positive binding energy), with E_b^i being the corresponding dislocation-solute binding energy and c_d^i being the average concentration of that carbon site bound to the dislocation. c_{bulk} is the carbon concentration in the bulk, with c_{nom} the nominal carbon concentration per Fe atom.

In a given volume V , the number of carbon sites along the dislocation cores is $N_d = \rho V/b$, with ρ the dislocation density, and the number of octahedral sites is $N_{\text{oct}} = 6V/a_{\text{bcc}}$. This imposes constraints on the carbon concentrations: $N_{\text{oct}}c_{\text{bulk}} + N_dc_d = N_{\text{oct}}c_{\text{nom}}/3$, where the factor of 3 is because there are three octahedral sites per Fe atom in the bcc lattice. Using this relation, equation 4 can be solved self-consistently to give the carbon concentration around the core, as a function of nominal carbon concentration and temperature. The nominal carbon concentration was taken to be the maximum solubility of ferrite in the DER region, 0.02 wt\% appm. Calculations of 10 and 1000 appm were also performed. The dislocation density was varied between 1×10^{12} , 1×10^{14} and 5×10^{15} .

2.5 Progression to Line Tension Model

From the atomistic calculations of the Peierls potential and carbon-dislocation binding energies, one can make a line tension model of a dislocation from which we can obtain the kink-pair formation energies as a function of stress and carbon content. This model views the dislocation as an elastic string which moves on the Peierls potential ΔE_P .

The dislocation is modelled as a discretised line, with layer labels j . The energy of the dislocation line is given by:

$$E_{LT} = \frac{K}{2} \sum_j (\vec{P}_j - \vec{P}_{j+1})^2 + \sum_j \Delta E_P(\vec{P}_j) + (\sigma \cdot \vec{b}) \times \vec{l} \cdot \vec{P}_j - \sum_{j,k} E_C(|\vec{P}_j - \vec{P}_k^C|),$$

where K is a constant calculated from the model, ΔE_P is the Peierls potential, σ is the stress applied and \vec{b} is the burger's vector, with the dislocation line sense given by \vec{l} . \vec{P}_j corresponds to the dislocation core position in a given layer. $E_C(|\vec{P}_j - \vec{P}_k^C|)$ is the binding energy of a particular carbon k , at position \vec{P}_k^C , to a dislocation positioned at \vec{P}_j . The kink-pair formation enthalpies can then be found using the NEB/String method, to find the transition barrier height.

3 Results

3.1 Peierls Potential

Comparison of 2d Peierls potentials of the $1/2\langle 111 \rangle$ screw dislocation between DFT and tight-binding can be found in figure 4. Data was interpolated using 2d cubic splines. "E", "H" and "S" correspond to easy, hard and split core positions respectively, with the latter also corresponding to atomic positions. The relative energies between the different core positions is smaller in tight-binding compared to DFT. This is an artifact in the model, which has been validated in NEB calculations of the $1/2\langle 111 \rangle$ screw dislocation Peierls barrier: the tight-binding Peierls barrier is approximately half that of DFT [15]. The split core as seen in tight-binding is reminiscent of EAM potentials, where the split core energy is lower than that of the hard core [11]. Some of this discrepancy can be attributed to the erroneous interaction term included by Itakura, as detailed above—interaction energies can become arbitrarily high, if not made independent of truncation limit—but likely, there are effects in DFT which are not encapsulated fully within tight-binding (or EAM), such as a lack of core electron repulsion.

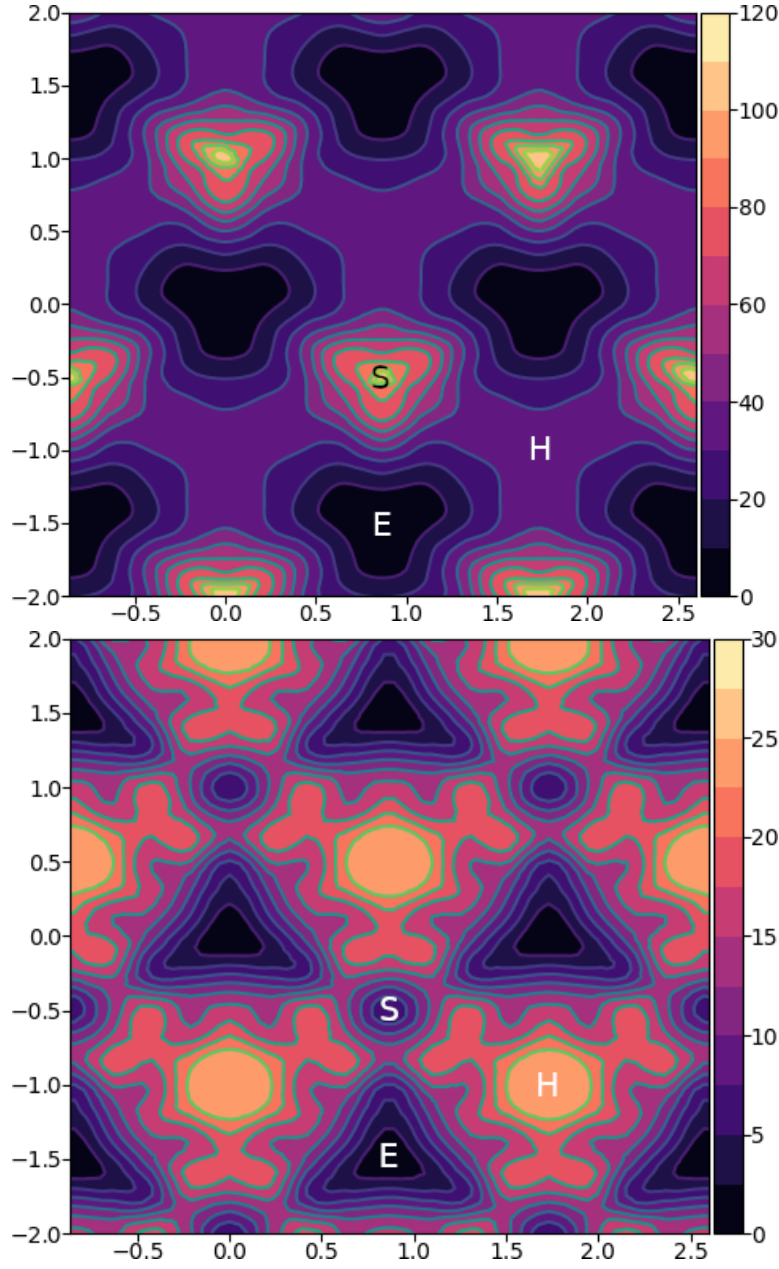


Figure 4: Comparison of 2d Peierls potentials of the $1/2\langle 111 \rangle$ screw dislocation between DFT [11] (top) and tight-binding (bottom). "E", "H" and "S" correspond to easy, hard and split core positions respectively, with the latter also corresponding to atomic positions. The relative energies between the different core positions is smaller in tight-binding compared to DFT. The split core as seen in tight-binding is reminiscent of EAM potentials, where the split core energy is lower than that of the hard core. The discrepancy is probably due to an insufficient repulsion at close range within the tight-binding model.

Pos	ΔE_{INT}	ΔE_{tbe}	ΔE_{P}	$\Delta E_{\text{P}}^{\text{DFT}}$
1	0	0	0	0
2	-0.7	7.3	7.9	3.2
3	-1.4	16.0	17.4	19.2
4	-2.0	22.2	24.2	31.1
5	-2.5	24.8	27.4	39.3
6	-3.3	3.0	6.3	11.5
7	-6.5	7.1	13.6	39.9
8	-9.6	13.0	22.6	75.2
9	-12.5	5.4	17.9	108.9
10	-4.8	22.1	26.9	34.8
11	-7.2	18.2	25.4	37.9
12	-9.8	14.0	23.8	60.7
13	-3.8	11.5	15.3	17.6
14	-6.9	15.1	22.0	29.9
15	-4.3	18.6	22.9	39.7

3.2 Preliminary calculations

To validate the cluster simulation method, the excess energy, defined as the difference in energy between a cell with a dislocation, and a perfect reference cell, was plotted as a function of $\ln(R/r_c)$, where $R = R_2$ of the cluster and $r_c = b$, as seen in figure 5. In elasticity theory, this should give a linear dependence where the gradient corresponds to combinations of elastic constants, with the y intercept corresponding to the core energy E_{core} . This is well reproduced by our model, except at low $\ln(R/r_c)$ as expected, where the cell size is not large enough to accommodate for sufficient relaxation of the dislocation core, increasing the core energy.

The core energy difference can be estimated by the difference between of excess energies between the easy and hard cores in the limit of $\ln(\frac{R}{R_0}) \rightarrow 0$. At the smallest measured value, one finds that the core energy difference $\Delta E_c^{\text{Easy-Hard}} = 76$ meV/b. This is in agreement with the results of Itakura [11], of 82 meV/b.

3.3 Fe-C binding energies

As found in DFT simulations by Ventelon [9], when a carbon was placed in the vicinity of a relaxed easy dislocation core—in either of the two nearest, distinguishable, octahedral sites—a spontaneous reconstruction of the dislocation core occurred: from easy to hard. Upon reconstruction, the dislocation core moved to a neighbouring triangle, when looking along the $\langle 111 \rangle$ direction, where the carbon found itself situated in the centre. This will be called a prismatic site, as in Ventelon’s paper. This model successfully reproduces this behaviour, confirming that both hard and easy dislocation cores

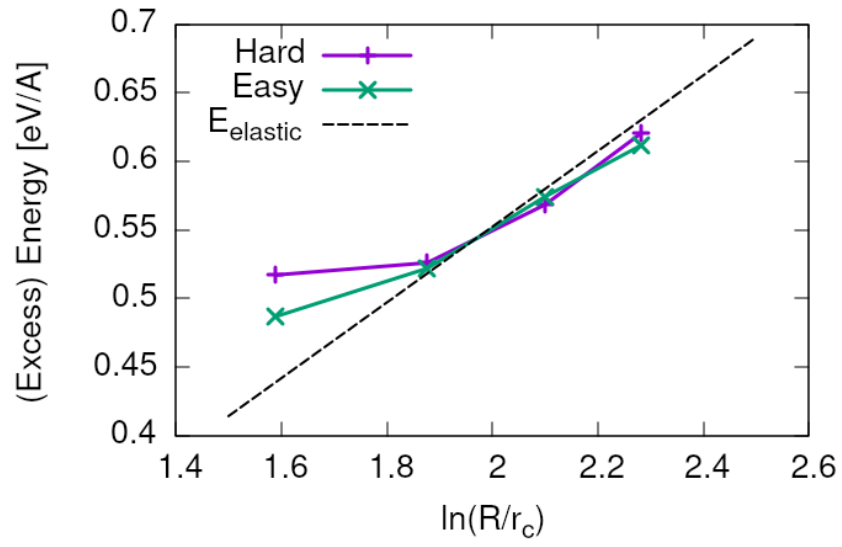


Figure 5: Excess energy of dislocation clusters with differing radii for both the easy and hard core configurations. The prediction from elasticity theory is given by the black, dashed line. Deviation of both cores occur when cell size is small, creating an increase in the core energy, which elasticity theory cannot account for.

must be studied to fully understand screw dislocation behaviour in bcc iron.

The binding energies of carbon to both the hard and easy cores can be seen in table 2, with the resulting distribution of carbon in figures 6 and 7.

The distribution of carbon strongly depends on the type of core it finds itself situated near. The easy core only significantly modifies the position of the iE1 site, to the E1 site, situated in the centre of an adjacent triangle. All other sites are unaffected, so there is a one-to-one correspondence between all iE j and E j sites, where $j \in \{2 \dots 10\}$. There are carbon basins available close to the core, but not inside.

Carbon favours a prismatic site within the hard core (H1), which has the highest binding energy, 1.29 eV, of all sites considered. There are no binding sites apparent in a triangular annulus (of width $a_{\text{bcc}}\sqrt{2}/2$) surrounding the hard core triangle due to the destruction/volume reduction of octahedral sites near the hard core. The initial octahedral sites, iH1 and iH2 decay to the H1 site. Similarly, iH3 and iH4 decay to the H2 site, with iH9 and iH10 decaying to a H7 site. Relations between each of the sites is given in table 1.

Table 1: Decay relations between the initial and final sites upon relaxation of carbon interstitials around the hard core.

Initial	Final
iH1, iH2	H1
iH3, iH4	H2
iH5	H3
iH6	H4
iH7	H5
iH8	H6
iH9, iH10	H7

Note that interactions between carbon atoms around the core are not taken into account here: figures 6 and 7 are purely diagrammatic and not what one expects the true distribution of carbon around a screw dislocation would be. Carbon is strongly repulsive at first nearest-neighbour distances, which would modify each of these distributions.

These binding energies agree well with experiment and previous calculations.

EAM calculations by Clouet [16, 17] found a maximum binding energy of 0.41 eV by calculating the elastic dipole tensor within Eshelby theory. Hanlummyuang *et al.* [18], similarly conducted DFT and EAM calculations for the interaction energy 12Å from the core, and their calculations agreed with the continuum limit of Eshelby theory with a binding energy of 0.2 eV.

In DFT calculations by Ventelon [9], the interaction energy of a carbon in a hard core prism configuration was found to be 0.79 eV for a thickness in the Z direction of $3b$ (0.73eV for $6b$)—in the convention that a positive bind-

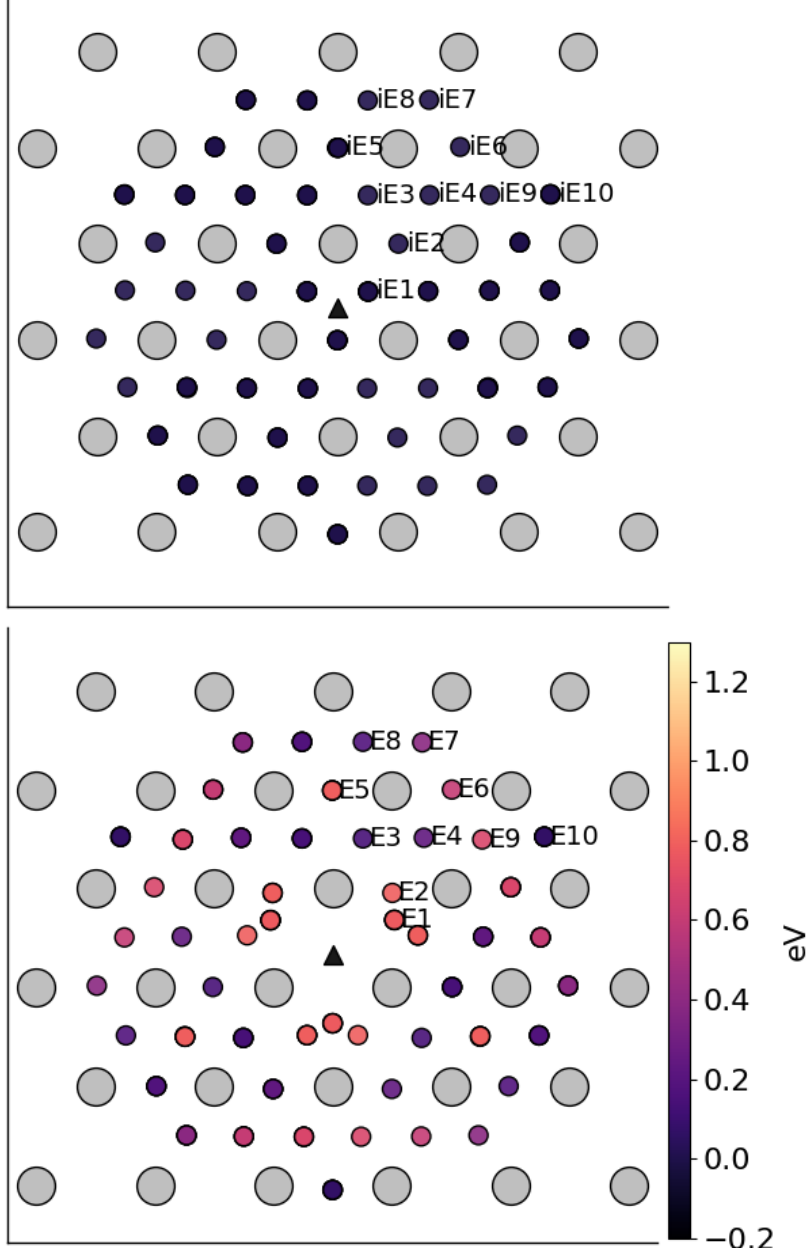


Figure 6: Initial (top) and final (bottom) positions and binding energies (eV) of carbon around the easy core. Binding energies are not shown for the initial positions. Top: initial positions before relaxation. Bottom: final positions and binding energies after relaxation. The core was constrained by fixing the top and bottom three atoms surrounding each of the cores. As shown by Ventelon [9], the first and second closest octahedral sites to the hard core decay to a prismatic position inside the hard core.

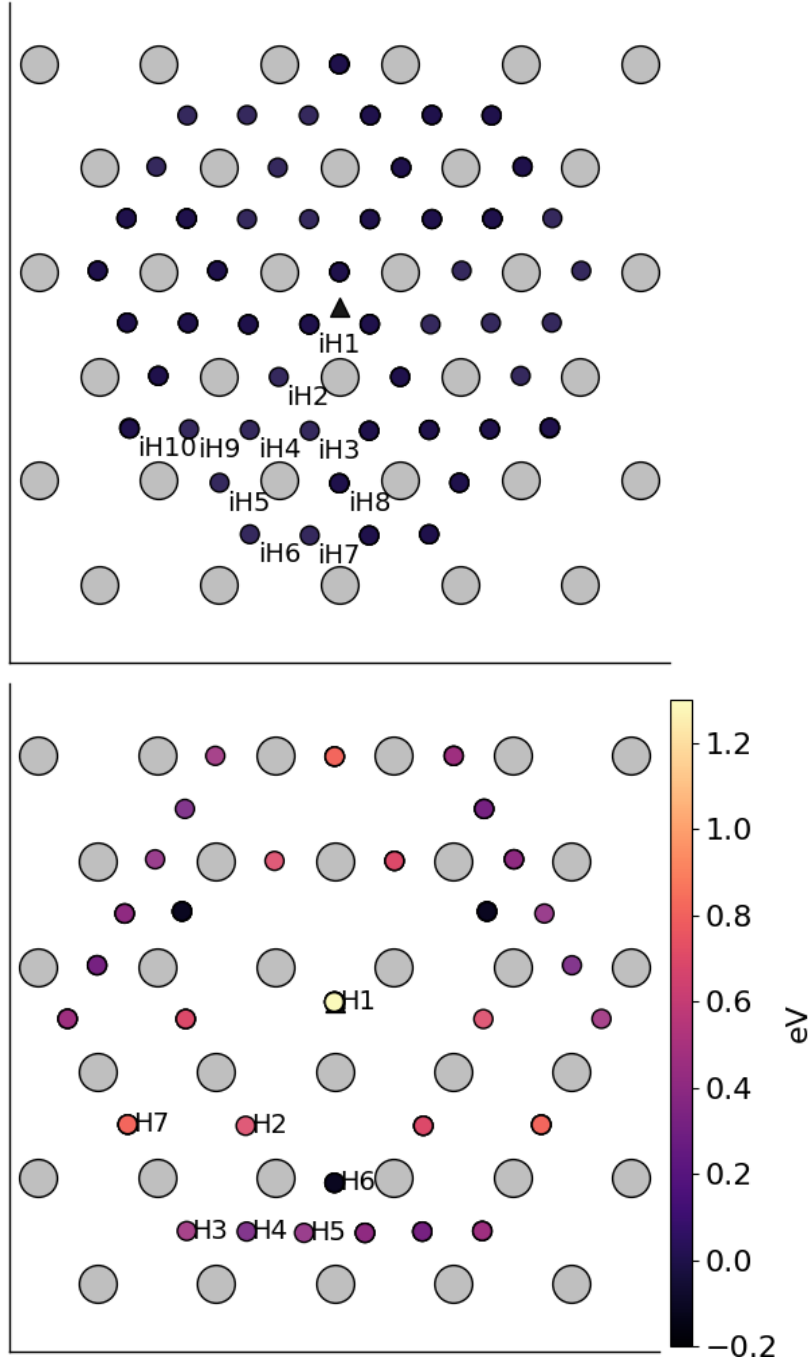


Figure 7: Initial (top) and final (bottom) positions and binding energies (eV) of carbon around the hard core. The core was constrained by fixing the three atoms surrounding each of the cores in the top and bottom layers. As shown by Ventelon [9], the first and second closest octahedral sites to the hard core decay to a prismatic position inside the hard core.

Site Type	distance from core [b]	E^z [eV]	ΔE^z [eV]	E_b [eV]	E_b^z [eV]
E1	0.57	0.185	-0.018	0.793	0.775
E2	0.70	0.202	-0.001	0.793	0.793
E3	0.99	0.205	0.002	0.137	0.139
E4	1.21	0.208	0.005	0.229	0.234
E5	1.36	0.210	0.008	0.784	0.791
E6	1.66	0.209	0.007	0.597	0.603
E7	1.89	0.206	0.003	0.385	0.388
E8	1.77	0.203	0.000	0.177	0.178
E9	1.52	0.201	0.000	0.683	0.683
E10	1.95	0.202	0.000	0.067	0.067
H1	0.00	0.196	-0.006	1.298	1.291
H2	1.19	0.210	0.007	0.691	0.698
H3	2.12	0.209	0.007	0.461	0.467
H4	1.91	0.207	0.005	0.311	0.316
H5	1.80	0.208	0.006	0.403	0.409
H6	1.40	0.207	0.005	-0.119	-0.114
H7	1.35	0.206	0.006	0.825	0.819

Table 2: Table of energies leading to the zero-point energy corrected binding energy using the cluster method for simulation of dislocation-carbon interactions.

ing energy indicates attraction. This is significantly lower than the 1.29eV interaction energy of tight-binding.

This discrepancy can be partially explained by the fact that the cells have not been allowed to relax with all degrees of freedom, as in the Ventelon results: the three atoms around the screw core are fixed in Z so the dislocation core position does not change upon relaxation. A larger source of error is likely from the fitting of the tight-binding model itself. The Peierls barrier of this s-d model of iron, necessary for Fe-C interactions, has been shown to be half that found in DFT, or the canonical d model [15], but the solution energies for Fe-C defect complexes are well described. This implies there is insufficient repulsion between Fe-Fe species, upon deformation, leading to a higher Fe-C binding energy from tight-binding, compared to DFT.

3.4 Analysis of carbon concentration along dislocation

Variation of carbon concentration along the dislocation line for each of the binding sites can be seen in figure 8. Due to the lower overall binding energies of carbon to the easy core, one sees that the concentration of weakly bound sites occurs at a lower temperature, as expected. Dislocation densities near the upper bound of what has been observed in martensite, from $\rho \approx 10^{15}$, reduce the temperature at which carbon concentration decreases around the

dislocation core. Lower nominal carbon concentrations cause carbon concentrations around the dislocation to decrease at a lower temperature.

In the operating temperature range of $40 - 90 \text{ deg C} = 310 - 360 \text{ deg K}$, we expect most of the hard core sites are saturated. Given the high concentrations of the E1/E2 sites around the easy core in this range, we expect all dislocations will be of the hard core type, due to reconstruction by carbon adjacent to the dislocation core.

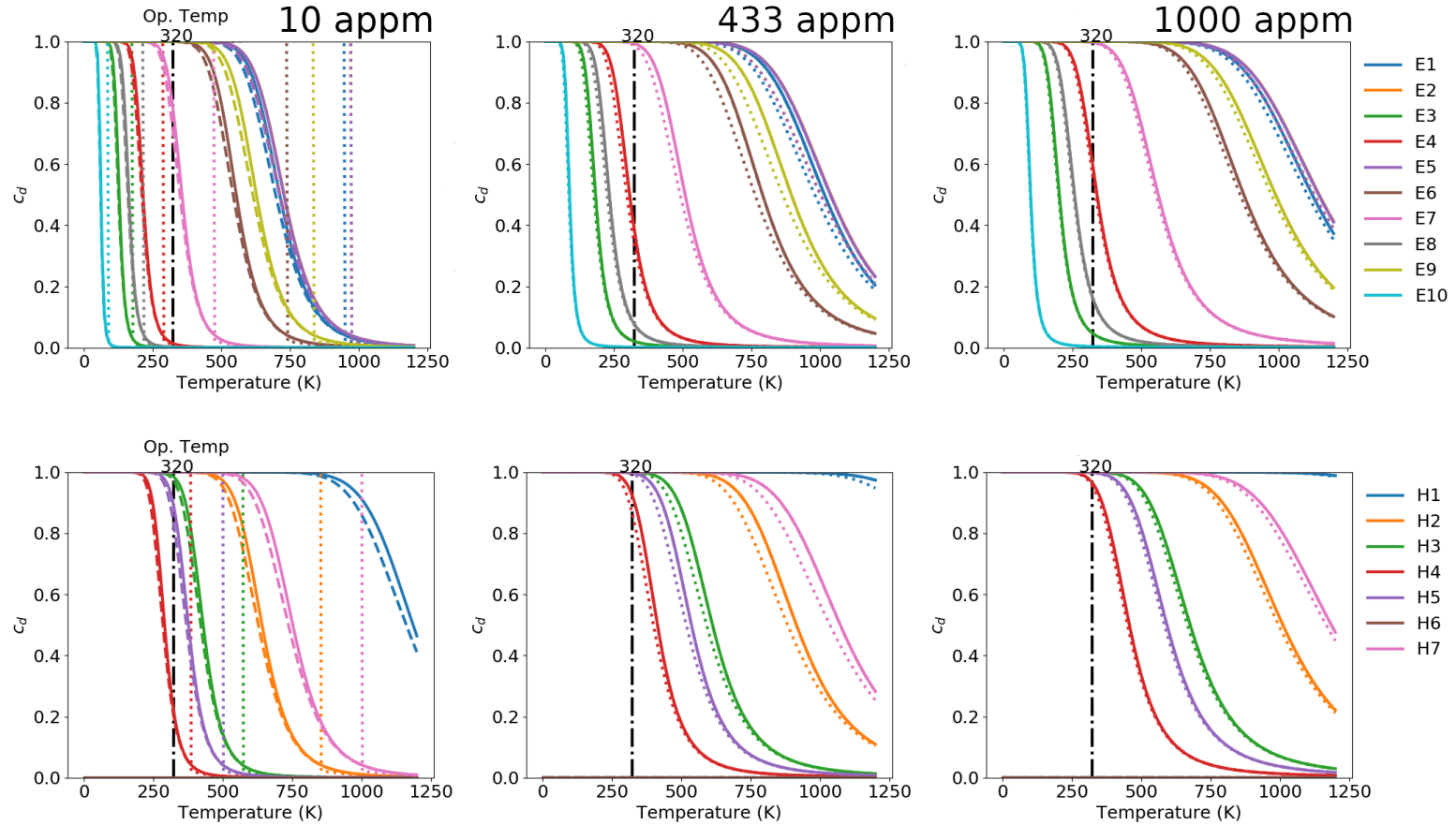


Figure 8: Variation of carbon concentration on the dislocation line c_d for each of the binding sites for the easy core (top) and hard core (bottom). Solid, dashed and dotted lined correspond to dislocation densities of 1×10^{12} , 1×10^{14} and 5×10^{15} respectively. The nominal carbon concentrations are 10 appm (left) and 1000 appm (right), with the middle figures taken to be the concentration of carbon at the solubility limit C in ferrite: $0.02\text{wt}\% \approx 433 \text{ appm}$. c_d and c_{bulk} reached self-consistency, with an absolute tolerance of 1×10^{-3} . C-C interactions were not taken into account. The concentration of carbon around the easy core, drops off at a lower temperature than that of the hard core due to lower binding energies, with reduction in concentration. The operating temperature is taken to be $50 \text{ deg C} = 320 \text{ deg K}$.

3.5 Progression to Line Tension Model

The K coefficient for the line tension model was calculated from atomistic simulations, using the prescription of Itakura [11], calculating a hessian from the displacement of atoms surrounding the dislocation core, giving results of $K = 0.734 \text{ eV}\text{\AA}^{-2}$, compared to DFT, where $K = 0.816 \text{ eV}\text{\AA}^{-2}$.

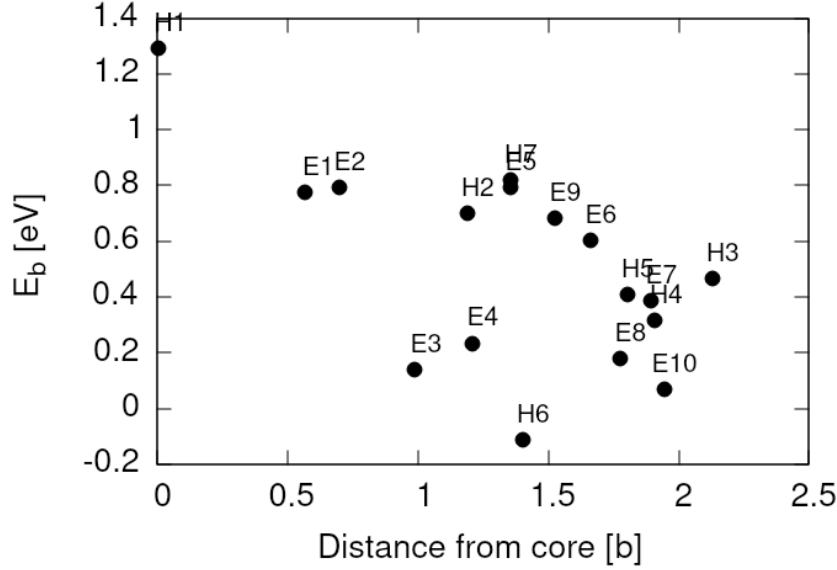


Figure 9: Distance dependence of the binding energies of carbon to the $1/2\langle 111 \rangle$ screw dislocation in iron. Positive binding energies denote a favourable binding.

The distance dependence of the dislocation-carbon binding energies, as seen in figures 9 and 10, can be fit by a single lorentzian, as was done in Itakura—but with the omission of many binding energies, as is done in Itakura [10]. The choice of sites used for the fitting is discussed in section 4.

Validation tests of the solute-dislocation interaction within the line tension model will be carried out on the Itakura data set for the binding of hydrogen to screw dislocations in bcc iron. This will be used to verify the kink-pair formation enthalpies stated in their paper (using the lorentzian form of the dislocation-solute interaction energy). This data set will also be used to verify the new interpolated solute-dislocation interaction energy, between the hard and easy core configurations.

4 Discussion

As in [19], carbon interactions are found to be vital in understanding how screw dislocations move in steels. Due to the spontaneous reconstruction of

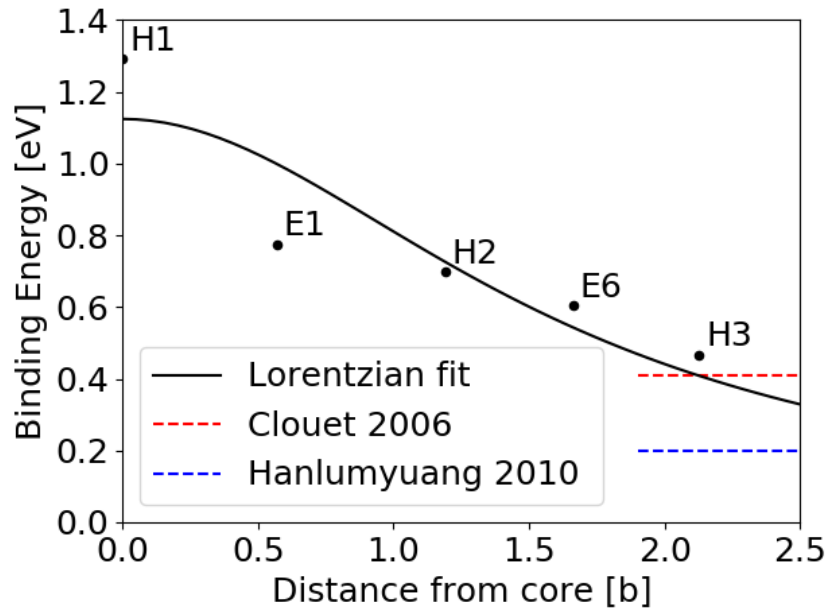


Figure 10: Fit of lorentzian to carbon-dislocation binding energies. The sites chosen to fit to were determined by those sites a prismatic carbon in a hard core configuration would find itself, if the dislocation were to move without it along the $X = \langle \bar{2}11 \rangle$ direction.

the easy core upon introduction of carbon, and the large binding energy of the H1 site, one would expect a hard core with carbon in a prismatic site as the ground state configuration for pinned dislocations.

In the context of dislocation-assisted carbon migration, with sufficient contact stress, dislocations in their hard core ground state will be forced to move (say, along the $X = \langle \bar{2}11 \rangle$ direction), which results in the hard core reconstructing to an easy core. Due to the much higher velocity of dislocations, relative to the diffusivity of carbon, carbon in the prismatic site stay in-place, becoming an E1 site. A drag force now acts to impede motion of the dislocation, due to the binding of the carbon in the E1 site. Progression of dislocation glide results in further reconstruction of the dislocation core to hard, easy and hard cores, with the original carbon being situated in H2, E6 and H3 sites respectively, relative to the dislocation centre. Thus as the dislocation moves, there is a significant drag force acting on the dislocation, which decreases the further the dislocation moves from carbon. The dependence of the binding energy to these sites can be seen in figure 10.

In normal operating temperatures of the bearing, one expects all dislocations to be hard cores saturated with carbon (neglecting C-C interaction) in most of the H j sites, as seen in the concentration analysis.

5 Future work

The prerequisites for a line tension model are in place for determination of the kink-pair formation enthalpies of screw dislocations as a function of carbon content and stress.

Using the kink-pair formation enthalpies and the binding energies of carbon to screw dislocations, one can proceed with kinetic Monte Carlo simulation of dislocation glide, in an environment of carbon to understand how dislocations can move carbon under applied stress, in different temperature and nominal carbon concentration regimes.

It would be of interest to pursue atomistic calculations of carbon bound to edge dislocations. Recent DFT/Eshelby theory calculations by Maugis *et al.* [20], show, counterintuitively, that under *compressive* stress, carbon diffusivity is *enhanced*. Pipe diffusion along edge dislocations could therefore be an important aspect to consider in carbon transport, in addition to the higher mobility edge dislocations in bcc iron. As such, edge dislocations could be quite important within the mechanism of dislocation-assisted carbon migration.

Ising and Monte Carlo models of intersite carbon interactions have been performed using the results of DFT carbon-dislocation binding energies [19]. These calculations only considered the hard core, with carbon binding sites of the H1 prismatic site and a H2 site, (which they name P and $O^{(4)}$ respectively in their paper). First neighbour C-C interactions were taken into account,

both along the dislocation line and between carbon sites. Using the tight-binding calculations detailed in this report, we can easily apply and extend this analysis to consider more binding sites around the hard core, and observe stable carbon distributions around the easy core.

6 Conclusion

Dislocation-assisted carbon migration is the mechanism by which martensite decays to form DER regions—composed of ferrite interspersed in a martensitic matrix—which enhances failure risk by RCF. There is dispute over where excess carbon from the martensitic matrix finds itself after decay. The current leading mechanism suggests carbon segregates to pre-existing carbides, yet recent experimental results show in the late stages of DER formation, pre-existing carbides are partially dissolved in areas of highly localized plasticity, implying segregation of carbon to dislocations. As such, a thorough investigation of carbon-dislocation interactions is vital to understanding how DER initially forms and progresses.

Tight-binding, atomistic simulations, the first stage in a multi-scale paradigm to understand dislocation-assisted carbon migration, found a peierls potential comparable to that of DFT results. Carbon distribution around the easy and hard cores were found differ significantly, with the largest binding energy being found by carbon being situated in a prismatic site in the hard core. Carbon within 3\AA of the easy core caused reconstruction to the hard core, with carbon in a prismatic site.

Equilibrium concentrations of carbon around the hard/easy cores at normal operating temperatures suggest that all dislocations are of hard core type with carbon situated in a H1 site, with reconstruction of all easy core dislocations to hard core, resulting in all dislocations being pinned.

If a dislocation moves under stress from the hard core-prismatic carbon ground state, a large drag force acts on the dislocation upon movement to adjacent easy and hard positions, as the carbon will stay in place due to its low diffusion coefficient, relative to dislocation velocity. The carbon-dislocation binding energies decrease with distance, and are in good agreement with literature.

Line tension and kMC models will be used to determine how dislocation glide is affected by carbon and how carbon can move with dislocations.

7 Appendix

7.1 Regularisation of interaction energy in quadrupolar array

In isotropic elasticity, the elastic energy of a single dislocation dipole in an infinite lattice is given by

$$E_{\text{el}}^{\infty} = \frac{\mu b^2}{4\pi} \ln\left(\frac{r}{r_c}\right)$$

The contribution from periodic images to the correction is

$$E_{\text{img}} = E_{\text{el}}(\mathbf{a}, \mathbf{c}_i, r_c) - E_{\text{el}}^{\infty}(\mathbf{a}, r_c),$$

"Ghost" dipoles are introduced to account for the conditional convergence of the sum at $\pm\alpha\mathbf{b}$ and $\pm\beta\mathbf{b}$, where $\alpha = \beta = 0.5$. We define $E_{\text{dg}}(\mathbf{R})$ as the interaction energy of a ghost dislocation and a dipole at \mathbf{R} anisotropic elasticity equations as shown in [21].

Defining,

$$E_{\text{dd}}(\mathbf{R}) = \frac{\mu b^2}{2\pi} \ln \frac{|\mathbf{R}|^2}{|\mathbf{R} + \mathbf{a}| \cdot |\mathbf{R} - \mathbf{a}|},$$

we obtain,

$$E_{\text{img}} = \frac{1}{2} \sum_{\mathbf{R}} [E_{\text{dd}}(\mathbf{R}) - E_{\text{dg}}(\mathbf{R})] - \frac{1}{2} E_{\text{dg}}(\mathbf{R} = 0),$$

which can be subtracted from the total energy as given from atomistic calculations, for a regularised interaction energy.

7.2 Zero-point energy calculation

After relaxation of the C-dislocation system, a 3x3 Hessian matrix is constructed by taking the numerical derivative of forces observed on the carbon atom after displacement by ± 0.015 in each of the X , Y and Z directions. The three atoms surrounding the core on the first and third layers were again fixed in Z coordinate. The zero-point energy is given by

$$E_z = \frac{1}{2} \sum_{i=1}^3 \frac{h}{2\pi} \sqrt{k_i/m_C},$$

where k_i are the eigenvalues of the Hessian and m_C is the mass of carbon.

8 Bibliography

References

- [1] H. Fu, E.I. Galindo-Nava, and P.E.J. Rivera-Díaz del Castillo. Modelling and characterisation of stress-induced carbide precipitation in bearing steels under rolling contact fatigue. *Acta Materialia*, 128:176–187, April 2017.
- [2] Hanwei Fu, Wenwen Song, Enrique I. Galindo-Nava, and Pedro E.J. Rivera-Díaz del Castillo. Strain-induced martensite decay in bearing steels under rolling contact fatigue: Modelling and atomic-scale characterisation. *Acta Materialia*, 139(nil):163–173, 2017.
- [3] Anurag Warhadpande, Farshid Sadeghi, and Ryan D. Evans. Microstructural alterations in bearing steels under rolling contact fatigue part 1—historical overview. *Tribology Transactions*, 56(3):349–358, May 2013.
- [4] Anurag Warhadpande, Farshid Sadeghi, and Ryan D. Evans. Microstructural alterations in bearing steels under rolling contact fatigue: Part 2—diffusion-based modeling approach. *Tribology Transactions*, 57(1):66–76, November 2013.
- [5] A. P. Voskamp and E. J. Mittemeijer. State of residual stress induced by cyclic rolling contact loading. *Materials Science and Technology*, 13(5):430–438, 1997.
- [6] H. Swahn, P. C. Becker, and O. Vingsbo. Martensite decay during rolling contact fatigue in ball bearings. *Metallurgical Transactions A*, 7(8):1099–1110, August 1976.
- [7] H. K. D. H. Bhadeshia. Solution to the bagaryatskii and isaichev ferrite–cementite orientation relationship problem. *Materials Science and Technology*, 34(14):1666–1668, May 2018.
- [8] A. T. Paxton and C. Elsässer. Analysis of a carbon dimer bound to a vacancy in iron using density functional theory and a tight binding model. *Physical Review B*, 87(22), June 2013.
- [9] Lisa Ventelon, B. Lüthi, E. Clouet, L. Proville, B. Legrand, D. Rodney, and F. Willaime. Dislocation core reconstruction induced by carbon segregation in bcc iron. *Physical Review B*, 91(22), June 2015.
- [10] M. Itakura, H. Kaburaki, M. Yamaguchi, and T. Okita. The effect of hydrogen atoms on the screw dislocation mobility in bcc iron: a first-principles study. *Acta Materialia*, 61(18):6857–6867, 2013.

- [11] M. Itakura, H. Kaburaki, and M. Yamaguchi. First-principles study on the mobility of screw dislocations in bcc iron. *Acta Materialia*, 60(9):3698–3710, May 2012.
- [12] Emmanuel Clouet. Screw dislocation in zirconium: An ab initio study. *Physical Review B - Condensed Matter and Materials Physics*, 86(14):1–11, 2012.
- [13] Vasily Bulatov. *Computer Simulations of Dislocations (Oxford Series on Materials Modelling)*. Oxford University Press, dec 2006.
- [14] P.M. Anderson, J.P. Hirth, and J. Lothe. *Theory of Dislocations*. Cambridge University Press, 2017.
- [15] E. Simpson. *A Tight Binding Study of Dislocations in Iron and Their Interactions with Hydrogen*. PhD thesis, King’s College London, 2019.
- [16] Emmanuel Clouet, Sébastien Garruchet, Hoang Nguyen, Michel Perez, and Charlotte S. Becquart. Dislocation interaction with c in -fe: A comparison between atomic simulations and elasticity theory. *Acta Materialia*, 56(14):3450–3460, August 2008.
- [17] C.S. Becquart, J.M. Raulot, G. Bencteux, C. Domain, M. Perez, S. Garruchet, and H. Nguyen. Atomistic modeling of an fe system with a small concentration of c. *Computational Materials Science*, 40(1):119–129, July 2007.
- [18] Y. Hanlunmyuang, P.A. Gordon, T. Neeraj, and D.C. Chrzan. Interactions between carbon solutes and dislocations in bcc iron. *Acta Materialia*, 58(16):5481–5490, September 2010.
- [19] B Lüthi, F Berthier, L Ventelon, B Legrand, D Rodney, and F Willaime. Ab initio thermodynamics of carbon segregation on dislocation cores in bcc iron. *Modelling and Simulation in Materials Science and Engineering*, 27(7):074002, July 2019.
- [20] P. Maugis and D. Kandaskalov. Revisiting the pressure effect on carbon migration in iron. *Materials Letters*, 270:127725, July 2020.
- [21] Wei Cai, Vasily V. Bulatob, Jinpeng Chang, Ju Li, and Sidney Yip. Periodic image effects in dislocation modelling. *Philosophical Magazine*, 83(5):539–567, January 2003.